Gain Enhancement in Cladding-Pumped Silicon Raman Amplifiers

Michael Krause, *Associate Member, IEEE*, Hagen Renner, Sasan Fathpour, *Member, IEEE*, Bahram Jalali, *Fellow, IEEE*, and Ernst Brinkmeyer

***Abstract*—Core-pumped silicon Raman amplifiers reported so far have exhibited gains of 4 dB or less in continuous-wave operation, limited by free-carrier absorption. Here we propose a device design that mitigates the problem of free-carrier absorption and leads to significantly higher gain values. In the new design, we surround the silicon waveguide with an additional rib-shaped passive cladding with a refractive index between that of silicon and the silica buffer. By injecting the pump power into the cladding, instead of directly into the silicon core, the overlap of the pump power with the silicon core is reduced and thus the effect of free-carrier absorption on the pump is weakened. The amplifier may therefore be made much longer, and higher total gains be achieved than in conventional core-pumped amplifiers. We present a detailed analysis of a design where a total gain as high as 18 and 34 dB may be achieved with pump powers of 300 mW and 1 W, respectively. We describe the model we have developed to design and optimize cladding-pumped silicon Raman amplifiers. Explicit expressions are formulated for the nonlinear effective areas for stimulated Raman scattering and two-photon absorption in silicon waveguides, taking into account the differing tensorial structures of these nonlinearities.**

***Index Terms*—Free-carrier absorption, Raman amplifiers, silicon nitride, silicon photonics.**

I. Introduction

THE field of silicon photonics has seen significant progress in the last few years [1], [2]. One of the many successes is that a viable optical gain mechanism has been found in the form of stimulated Raman scattering (SRS), which is the optical amplification of a signal or "Stokes" wave in the presence of a strong pump wave. By injecting the signal and the pump into the core of a silicon waveguide, one can thus obtain a silicon Raman amplifier (SRA) [3]–[8]. Furthermore, the Raman effect has also been used to successfully realize lasers [9], [10] and wavelength converters [11] in silicon.

In principle, SRS amplification is possible for all wavelengths where silicon is transparent, i.e., from 1.2 μm towards longer wavelengths, as long as a suitable pump source is available: for SRS to work, the optical frequency of the pump wave must be larger than that of the Stokes wave by an amount that depends on the material—in silicon, the "Raman shift" is approximately 15.6 THz [3]. This spectral freedom is in contrast to amplifiers based on rare-earth dopants such as erbium-doped waveguide amplifiers (EDWAs) [12], which are restricted to a rather narrow signal-wavelength range. One particularly promising use of SRAs is therefore in the form of compact stand-alone amplifier modules for optical-communications wavelengths that are not covered by EDWAs (for example, the 1300-nm band). The devices proposed in this paper are meant for such applications. Because of their very long waveguide lengths, our devices are not suitable for integration with CMOS and, hence, we are not proposing them as amplifiers for on-chip optical interconnects.

After the first experimental demonstration of SRS in a silicon waveguide in 2003 [3], SRAs have been improved to the point that gains of up to 4 dB under continuous-wave (CW) operation have been demonstrated [8]. A further increase of the gain is currently limited by nonlinear absorption effects that set in at high pump powers: two-photon absorption (TPA) generates free charge carriers in the silicon-waveguide core which accumulate and lead to significant additional optical losses, namely free-carrier absorption (FCA) [13]. As a result, it does not help to simply increase the pump power indefinitely; for each SRA there is a certain pump power beyond which the amplifier gain will decrease again. The maximum possible gain for a given waveguide technology is only achieved for a single optimal amplifier length and pump power [14].

To mitigate the problem of FCA and increase the gain of SRAs, several approaches have been used. On the one hand, the lifetime of the TPA-generated charge carriers can be reduced by implantation of helium [15], argon [16] or oxygen [17], or the carriers can be extracted from the silicon core by means of an externally applied electric field in a p-i-n junction [8], or by exploiting the built-in field of the junction [18]. However, such a carrier sweep-out is only partially effective because at high pump intensities, the TPA-generated carriers screen the junction field and render the diode ineffective [19]. Exponential tapering of the effective mode area would permit arbitrary total gain, but is limited by the minimum effective area practically achievable [20]. On the other hand, we have recently proposed a cladding-pumped amplifier structure, in which the pump power is injected not directly in the silicon core but in an additional surrounding cladding without significant nonlinear absorption [21]. The pump power is then attenuated less by FCA due to the smaller overlap of the pump mode with the silicon core, and the entire amplifier can be made longer, thus delivering more gain. Drawbacks of the design presented in [21], however, are the large silicon-core dimensions which require large pump powers for achieving Raman gain. Furthermore, both the core and the

Manuscript received August 20, 2007; revised February 21, 2008.

M. Krause, H. Renner, and E. Brinkmeyer are with the Technische Universität Hamburg-Harburg, Optische Kommunikationstechnik, D-21073 Hamburg, Germany (e-mail: m.krause@tu-harburg.de).

S. Fathpour and B. Jalali are with the University of California, Los Angeles, Optoelectronics Circuits and Systems Laboratory, Los Angeles, CA 90095-1594 USA (e-mail: jalali@ucla.edu).

Digital Object Identifier 10.1109/JQE.2008.923427

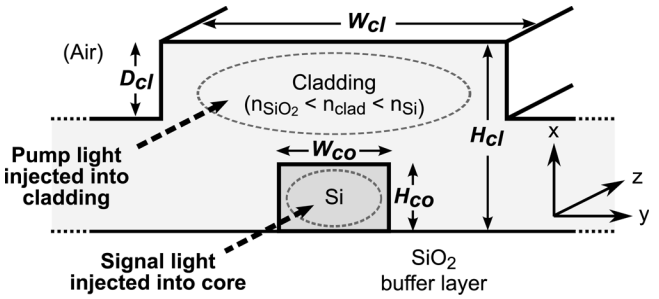

Fig. 1. Waveguide cross section for the proposed cladding-pumped silicon Raman amplifier.

rectangular cladding in [21] are heavily multimoded, which can in practice result in undesired mode interference, leading to excessive TPA and thus FCA.

In this paper, we present an improved design for a cladding-pumped silicon Raman amplifier operating in the 1300-nm (O-band) region, and we provide details on our full-vectorial mathematical model. The improved design includes a rib structure for the cladding waveguide that judiciously removes all undesired higher order modes. By using reduced cross-sectional dimensions compared to the design presented in [21], we show that it is possible to achieve CW gains exceeding 30 dB with pump powers on the order of 1 W.

The outline of the paper is as follows. Section II introduces the geometry of the cladding-pumped silicon Raman amplifier and the model we use to simulate and optimize these devices. Section III introduces a particular design exhibiting significantly increased gain compared to conventional core-pumped SRAs and discusses the mechanisms that support the gain enhancement. Section IV analyzes the influence of deviations from the ideal design specifications, and Section V studies the gain as a function of the linear losses and the effective carrier lifetime. Finally, Section VI concludes the paper, and Appendixes A and B present further details of our mathematical model.

II. Geometry and Model

A. Geometry

Fig. 1 schematically shows the waveguide cross section for a cladding-pumped silicon Raman amplifier. The proposed structure consists of a rectangular silicon waveguide core on top of a silica buffer layer. It is covered by a rib-shaped cladding the refractive index of which lies between that of silica and silicon, i.e., $n_{\mathrm{SiO_2}} < n_{\mathrm{clad}} < n_{\mathrm{Si}}$. In the simulations for this paper, we use a refractive index of $n_{\mathrm{clad}} = 2.0$, corresponding to silicon nitride [22], which can be integrated relatively easily with the processing of the rest of the structure. Materials with a similar refractive index that could be used alternatively are tantalum pentoxide or titanium dioxide.

The signal light to be amplified at the Stokes wavelength is guided in the fundamental mode of the entire structure, which is highly confined to the silicon core. While in a conventional core-pumped SRA [3]–[8], the pump power is also injected into the core, we here propose to inject the pump light in the only higher order mode of the structure, which is mainly guided in the cladding. Fig. 2(a) and (b) shows the mode-intensity profiles for a possible choice of the Stokes and pump modes, respectively. By using a rib-shaped cladding, we make sure that only these two desired modes (and their orthogonally polarized, though unused, counterparts) are guided by the structure.

In order to launch the pump and Stokes beams into the cladding-pumped amplifier, the Stokes waveguide (silicon core) could at some point be sharply curved by 90 degrees and routed away from under the cladding rib waveguide. Then standard techniques can be used to launch the Stokes light into the bare silicon core, while the pump power can be injected by focusing it onto the large lobe of the remaining rib waveguide made from the pure cladding material. At that point where the silicon core joins perpendicularly the pump waveguide, the pump will suffer small diffraction losses, but the length of this transition region can be kept on the order of a few micrometers by making use of the sharp bending radii that are possible for the silicon waveguide. In fact, we have found that it is most important to avoid an adiabatic passage of the silicon core from under the rib to the outside region because then the cladding pump mode is dragged along with the silicon core, and pump power can then not be injected as described above.

B. Differential Equations

In our model, the CW pump and Stokes powers $P(z)$ and $S(z)$ evolve along the waveguide according to the differential equations [23], [24]

$$\frac{1}{P}\frac{dP}{dz} = -\alpha_p - \frac{\lambda_s}{\lambda_p} g \frac{S}{A^{(\mathrm{SRS})}} - \beta_{\mathrm{pp}} \frac{P}{A_{\mathrm{pp}}^{(\mathrm{TPA})}} - \frac{\lambda_s}{\lambda_p} \beta_{\mathrm{sp}} \frac{2S}{A_{\mathrm{sp}}^{(\mathrm{TPA})}} - \eta_p \bar{\varphi} \lambda_p^2 \bar{N} \tag{1}$$

$$\frac{1}{S}\frac{dS}{dz} = -\alpha_s + g \frac{P}{A^{(\mathrm{SRS})}} - \beta_{\mathrm{ss}} \frac{S}{A_{\mathrm{ss}}^{(\mathrm{TPA})}} - \beta_{\mathrm{sp}} \frac{2P}{A_{\mathrm{sp}}^{(\mathrm{TPA})}} - \eta_s \bar{\varphi} \lambda_s^2 \bar{N} =: \gamma(z) \tag{2}$$

where z is the longitudinal coordinate and the five terms on the right-hand sides of (1)–(2) represent, respectively, linear losses, SRS, degenerate TPA, nondegenerate TPA, and FCA.

The linear loss coefficients at the pump and Stokes wavelengths λ_p and λ_s are given by α_p and α_s, respectively. The remaining physical quantities involved in (1)–(2) are explained in detail in Section II-C–E.

C. Stimulated Raman Scattering (SRS)

The strength of SRS is expressed in (1)–(2) as the ratio of the Raman-gain constant of bulk silicon, g, and the effective area $A^{(\mathrm{SRS})}$ that describes the influence of the waveguide geometry. For waveguides with the usual orientation, namely along the [011] direction on a (100) surface [25], [8], this effective area takes the form [see (35) in Appendix A]

$$A^{(\mathrm{SRS})} = \frac{4 Z_0^2 \hat{N}_p \hat{N}_s}{n_p n_s} \left\{ \int_{\mathrm{Si}} |\mathbf{e}_p|^2 |\mathbf{e}_s|^2 + |\mathbf{e}_p \cdot \mathbf{e}_s|^2 - 2\left(e_s^x\right)^2 \left(e_p^x\right)^2 - \left[\left(e_s^y\right)^2 - \left(e_s^z\right)^2\right] \cdot \left[\left(e_p^y\right)^2 - \left(e_p^z\right)^2\right] dA \right\}^{-1} \tag{3}$$

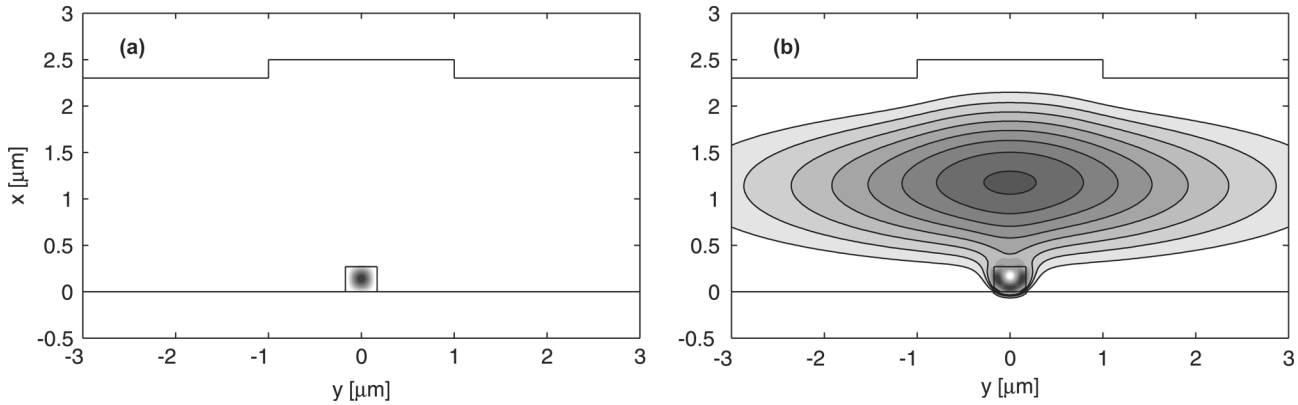

Fig. 2. (a) Mode-intensity profiles of the Stokes and (b) pump of a cladding-pumped silicon Raman amplifier. While the Stokes light to be amplified is guided in the silicon core, the pump mode is guided mainly in the (nonabsorbing) cladding and is thus scarcely attenuated by FCA.

where Z_0 is the vacuum impedance, $n_{p,s}$ are the (linear) refractive indexes of silicon at the pump and Stokes wavelengths, $\mathbf{e}_{p,s}$ are the electric fields of the pump and Stokes modes with real transverse and imaginary longitudinal components, and $\hat{N}_{p,s}$ are the corresponding mode normalizations

$$\hat{N}_i = \frac{1}{2}\int_{A_\infty} [\mathbf{e}_i(x,y) \times \mathbf{h}_i^*(x,y)] \cdot \hat{\mathbf{z}}\, dA \tag{4}$$

where $\mathbf{h}_{p,s}$ are the magnetic fields of the modes, $\hat{\mathbf{z}}$ is the unit vector in the propagation direction z, and the integration is over the entire transverse plane A_∞. In (3), we use superscripts to denote the cartesian components of the fields with respect to the coordinate system defined in Fig. 1, and $|\mathbf{e}_i|^2 = \mathbf{e}_i \cdot \mathbf{e}_i^*$, the asterisk denoting complex conjugation. The factor of λ_s/λ_p in front of the second term on the right-hand side of (1) expresses photon-number conservation.

D. TPA

Similar to the SRS gain, the attenuation caused by TPA is expressed in (1)–(2) in terms of the bulk-silicon TPA coefficients and certain effective areas.

On the one hand, the material parameters $\beta_{\rm pp}$ and $\beta_{\rm ss}$ are the degenerate-TPA coefficients of silicon at the pump and Stokes wavelengths, respectively. $\beta_{\rm sp}$ is the nondegenerate (pump↔Stokes) TPA coefficient "seen" by the Stokes wave, and the factor of λ_s/λ_p in front of the fourth term on the right-hand side of (1) expresses the fact that photons are removed from the pump and Stokes beams in equal numbers by nondegenerate TPA.

On the other hand, the three effective areas for TPA occurring in (1)–(2) are given by [see (27) in Appendix A]

$$A_{ij}^{(\rm TPA)} = \frac{4Z_0^2\hat{N}_i\hat{N}_j}{n_i n_j}\left\{\frac{1}{3}\int_{\rm Si} |\mathbf{e}_i|^2|\mathbf{e}_j|^2 + |\mathbf{e}_i\cdot\mathbf{e}_j|^2 + |\mathbf{e}_i\cdot\mathbf{e}_j^*|^2\, dA\right\}^{-1} \tag{5}$$

which we have derived under the assumption that the $\chi^{(3)}$ tensor describing TPA in silicon is isotropic and fulfills the Kleinman symmetry condition [26] (see the discussion in Appendix A).

E. FCA

In this Section we will derive an expression for the charge-carrier density $\bar{N}$ that occurs in the last terms describing FCA on the right-hand sides of (1)–(2).

As we are dealing with optically generated charge carriers without externally applied electric fields, the carrier dynamics are well described by ambipolar diffusion [27], [28], i.e., the electron and hole densities may be assumed to be equal at each point as in [13] and [29]. Furthermore, we assume that the optical powers $P(z)$ and $S(z)$ in the waveguide vary slowly enough along the propagation direction z such that the carrier-generation rate and thus the steady-state carrier density vary with z only on a scale large compared to the carriers' diffusion length. This reduces the carrier-diffusion problem to a locally two-dimensional process taking place only in the transverse cross-sectional plane (x, y) of the waveguide. The steady-state carrier density $N(x, y)$ then obeys the diffusion equation [27]

$$D\nabla^2 N + G - \frac{N}{\tau_b} = 0 \tag{6}$$

where D is the ambipolar diffusion constant, $G(x, y)$ is the local TPA carrier-generation rate, and τ_b is the bulk carrier lifetime. At the interfaces between silicon and the surrounding waveguide materials, N fulfills the boundary condition

$$D\,\mathbf{n}\cdot\nabla N = -SN \tag{7}$$

where $\mathbf{n}$ is a unit vector normal to the interface and directed outward, and S is the recombination velocity at the interface.

In order to solve (6)–(7) for the carrier density $N(x, y)$ exactly, we need to know the local carrier generation rate $G(x, y)$. The spatial distribution and the magnitude of the generation rate $G(x, y)$ will depend on the field shapes and powers of the pump and Stokes modes. However, a simple general solution for N can be obtained when we assume, as in [29], that the carrier diffusion is so fast that the steady-state carrier density N is constant, $N(x, y) = \bar{N}$, in those regions of silicon where the mode fields are concentrated. Consequently, the solution of (6)–(7) does not depend on where exactly the carriers are generated in the waveguide cross section, but only on how many of them are generated in total. Mathematically

$$\bar{N} = M \cdot \int_{\rm Si} G(x,y)\, dA = MG_{\rm tot} \tag{8}$$

where $G_{\rm tot}$ is the total number of carriers generated through TPA in the entire cross section of the waveguide per unit time and per unit waveguide length, and M is a constant of proportionality with unit s/m^2 which depends only on the waveguide geometry and the two material parameters, bulk recombination lifetime τ_b and interface recombination velocity S. The constant M can be related to the effective carrier lifetime of the waveguide, see Appendix B.

The total generation rate $G_{\rm tot}$ occurring in (8) can be derived by considering a thin slice Δz of the waveguide. The differential equations (1)–(2), rewritten in terms of photon fluxes, then show how many photons are absorbed by TPA in that slice per unit time. Finally, by requiring that for each two absorbed photons, an electron–hole pair is generated, an expression for $G_{\rm tot}$ is obtained. As a result, the free-carrier density $\bar{N}$ is given by

$$\bar{N} = \frac{M}{2h}\left[\frac{\beta_{\rm pp}P^2}{\nu_p A_{\rm pp}^{\rm (TPA)}} + \frac{\beta_{\rm ss}S^2}{\nu_s A_{\rm ss}^{\rm (TPA)}} + \frac{4\beta_{\rm sp}PS}{\nu_s A_{\rm sp}^{\rm (TPA)}}\right] \tag{9}$$

where h is Planck's constant, $\nu_{p,s} = c/\lambda_{p,s}$ are the optical frequencies of the pump and Stokes waves, and c is the speed of light in vacuum. The last term in brackets in (9) results from the two nondegenerate TPA contributions to (1)–(2) and can alternatively be written in the equivalent form $4\beta_{ps}PS/[\nu_p A_{\rm sp}^{\rm (TPA)}]$, where $\beta_{ps} = (\lambda_s/\lambda_p)\beta_{\rm sp}$ is the nondegenerate TPA coefficient for the pump wave, see Appendix A.

Finally, the FCA "seen" by the pump and Stokes waves is given by $\eta_{p,s}\bar{\varphi}\lambda_{p,s}^2\bar{N}$, where $\bar{\varphi} = 6 \times 10^{-10}$ [13] and $\eta_{p,s}$ are confinement factors quantifying the overlap of the modes with the silicon core

$$\eta_{p,s} = \frac{n_{p,s}}{2Z_0\hat{N}_{p,s}}\int_{\rm Si}|\mathbf{e}_{p,s}|^2\,dA \tag{10}$$

which corresponds to the standard perturbation result for the modal attenuation caused by an absorbing waveguide profile [30].

F. Simulation Parameters

Throughout this paper, we assume pump and Stokes wavelengths of $\lambda_p = 1220$ nm and $\lambda_s = 1303$ nm, respectively, which are separated by the silicon Raman shift of 15.6 THz. For the refractive indexes of silicon and silica, we evaluate the standard Sellmeier formulas at 1220 nm giving $n_{\rm Si} = 3.516$ and $n_{\rm SiO_2} = 1.447$, respectively [31], [32].

For the three TPA coefficients we use the values $\beta_{\rm pp} = 1.10$ cm/GW, $\beta_{\rm sp} = 1.00$ cm/GW and $\beta_{\rm ss} = 0.95$ cm/GW, which have been obtained from the model of [33] calibrated such that the degenerate-TPA coefficient at a wavelength of 1427 nm has a rather high value of 0.7 cm/GW [13], so that we do not underestimate the effects of nonlinear absorption. The values thus obtained are in the range of those recently reported for the 1200-nm region [34], [35]. For the Raman-gain coefficient we use the value $g = 23.6$ cm/GW, which corresponds to a value of 20 cm/GW at a pump wavelength of 1427 nm, assuming a $1/\lambda_s$ scaling law as in [36].

We use a full-vectorial mode solver [37] to calculate the modes of the various analyzed structures of the type shown in Fig. 1. We choose the predominantly y-polarized fundamental mode for the Stokes mode, and the next-higher order predominantly y-polarized mode for the pump (cladding) mode. Using (3), (5), and (10) we then calculate the effective areas and confinement factors required for the simulation of the amplifier characteristics on the basis of (1)–(2).

G. Solution of the Model Equations

The ordinary differential (1)–(2) can be integrated numerically for a given input pump power $P(0) = P_0$ and input Stokes power $S(0)$ from $z = 0$ to $z = L$. The total gain of the amplifier can then be calculated from

$$G = \frac{S(L)}{S(0)}. \tag{11}$$

We assume unsaturated operation of the amplifier in the remainder of this paper, i.e., the Stokes powers are so small that the longitudinal evolution of the pump power is not significantly influenced by them. Still, in general the gain of the amplifier must be calculated numerically. However, generalizing the results obtained in [14] it can be shown that for given material parameters and fixed Stokes and pump modes, the unsaturated gain of the cladding-pumped amplifier is maximized only when choosing a specific optimal amplifier length and optimal pump power. This maximum possible gain as well as the corresponding optimal length and pump power can be derived in explicit form, which can significantly speed up the optimization process.

III. Gain Enhancement in Cladding-Pumped SRAs

We now proceed to quantitatively illustrate how the concept of the cladding-pumped silicon Raman amplifier can increase the gain compared to conventional core-pumped amplifiers. Later in Section III-D we will explain the reason for the increased gain.

While in the previously presented design for a cladding-pumped silicon Raman amplifier [21] we used a highly multimode silicon core with dimensions of 2.0×1.5 μm^2, in this section we will discuss a new design with much smaller core dimensions of $W_{\rm co} = 350$ nm and $H_{\rm co} = 270$ nm. These dimensions are such that with an infinite upper cladding, the waveguide would support only the fundamental mode (in the two polarizations). With a rib-shaped upper cladding (as in Fig. 1), the structure may guide additional modes. We will show that the rib can be designed such that there is only *one* additional mode with the power mainly guided in the cladding, which is the one we will use as the pump mode, compare Fig. 2(b).

A. Maximum Possible Gain

In order to illustrate the potential of the cladding-pumped silicon Raman amplifier, we first consider the maximum gain that is possible with the structure for given material parameters and unlimited pump power, and compare the result with the core-pumped case. In Section III-G, we will consider practical limitations on the pump power.

Consider first the core-pumped case. We assume that the linear losses of the fundamental mode of the structure (used for both the pump and the Stokes power) are $\alpha_s = 2.0$ dB/cm, and that the effective free-carrier lifetime is $\tau_{\rm eff} = 1$ ns. These

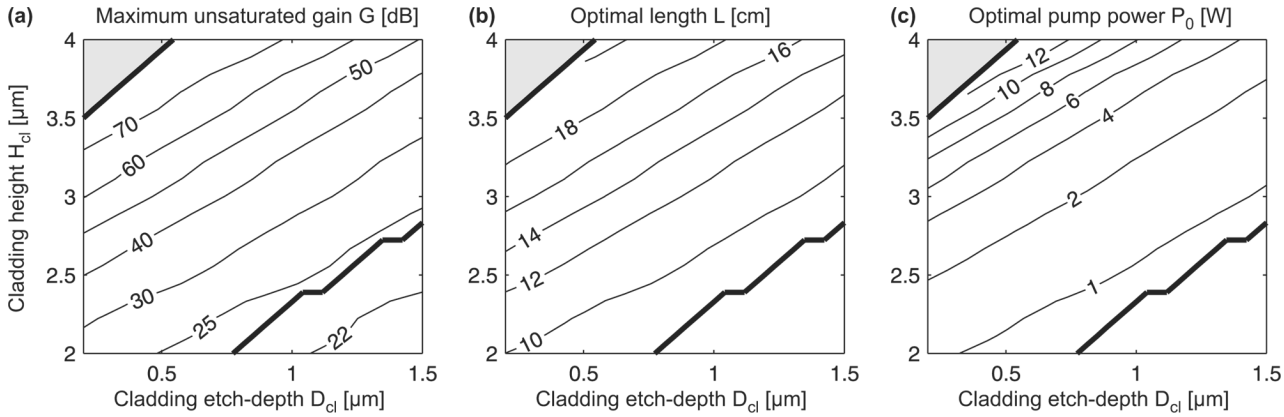

Fig. 3. For unlimited pump power: (a) maximum possible gain G of cladding-pumped silicon Raman amplifiers versus cladding height $H_{\rm cl}$ and etch depth $D_{\rm cl}$, and (b) the corresponding optimal lengths and (c) pump powers. If the pump power were injected directly into the silicon core, the maximum possible gain would be only 6.1 dB. The thick solid lines enclose the region where the structure guides only the two desired Stokes and pump modes shown in Fig. 2 and no higher order modes.

are typical values for silicon waveguides of the considered dimensions [4], [38], [6]. Using the approach described in Section II-G, we find that the maximum possible gain that can be achieved by core-pumping this waveguide is 6.1 dB, which is attained only for the optimal amplifier length of 2.6 cm and the optimal pump power of 350 mW. More pump power than this can not be usefully employed here, as the amplifier gain will then decrease [14].

Now we turn to the present case of cladding pumping. We assume that the linear losses of the pump mode are lower than those of the Stokes mode, namely only $\alpha_p = 0.5$ dB/cm, since the scattering losses are usually the smaller the larger the waveguide is (however, as we show in Section V, the cladding-pumped SRA is superior for equal pump and Stokes loss coefficients as well, see Fig. 10). When we arbitrarily choose a cladding rib width of $W_{\rm cl} = 1.5$ μm, we still have the two unspecified parameters cladding height $H_{\rm cl}$ and etch depth $D_{\rm cl}$. Fig. 3(a) shows the maximum possible gain of the cladding-pumped amplifier as a function of these two parameters, while Fig. 3(b) and (c) show the corresponding optimal lengths and pump powers, respectively.

As can be seen in Fig. 3(a), the maximum possible gain of the cladding-pumped amplifiers is significantly higher than the mere 6.1 dB achievable with the corresponding core-pumped amplifier for all considered choices of the cladding rib height $H_{\rm cl}$ and etch depth $D_{\rm cl}$. For example, for a cladding height of $H_{\rm cl} = 3.0$ μm and an etch depth of $D_{\rm cl} = 0.75$ μm, the maximum possible unsaturated gain is 40 dB. For this gain to be achieved, the amplifier must be 13 cm long and supplied with a pump power of 2 W. Also, there is considerable design freedom: amplifiers with the same gain can be obtained for all other rib dimensions along the 40-dB contour line in Fig. 3(a), while the required amplifier lengths and pump powers remain approximately the same, because the contour lines in Fig. 3(a)–(c) follow similar paths.

B. Single-Mode Claddings

The two thick lines in each of Fig. 3(a)–(c) enclose the region of cladding dimensions for which the structure has no modes other than the desired fundamental mode for the Stokes light

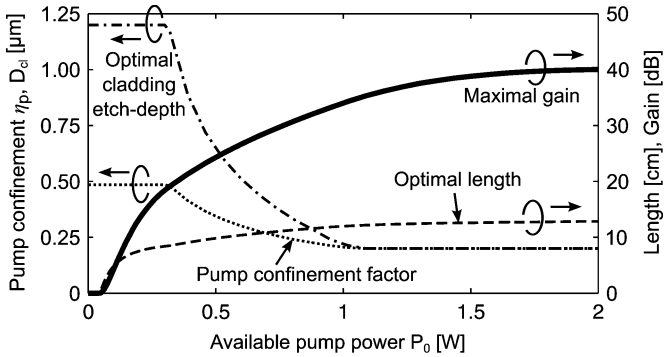

Fig. 4. Maximum possible gain (solid) of cladding-pumped amplifiers as a function of the available pump power for a fixed cladding height $H_{\rm cl} = 2.5$ μm. Also shown is the optimized amplifier length L (dashed), the optimized cladding etch-depth $D_{\rm cl}$ (dashed-dotted) and the corresponding pump confinement factor η_p (dotted).

in the core and a second-order mode for the pump light mainly guided in the cladding, as shown in Fig. 2. In the region above the upper-left thick line in Fig. 3, no guided mode other than the fundamental mode exists, and the pump power can then not be guided by the cladding.

A cladding with only a single pumping mode is desirable for two reasons. On the one hand, it makes it possible to cleanly launch the pump power into the cladding. If more guided modes were excited, these could produce an irregular interference pattern inside the silicon core. In the peaks of this pattern, TPA and thus FCA would be particularly strong, and the amplifier would deliver less total gain than possible if only one pump mode were present.

On the other hand, even if the launching conditions were such that in a multimode cladding only the desired pump mode was excited, the same undesired interference effects could occur because waveguide irregularities could eventually couple the pump light between different modes. This coupling would be particularly strong between the various cladding modes, because they lie closest to each other in k space ($n_{\rm SiO_2} = 1.447 < n_{\rm eff} < 2.0 = n_{\rm clad}$) and usually low-frequency irregularities predominate. By using a rib-shaped cladding, the higher order cladding

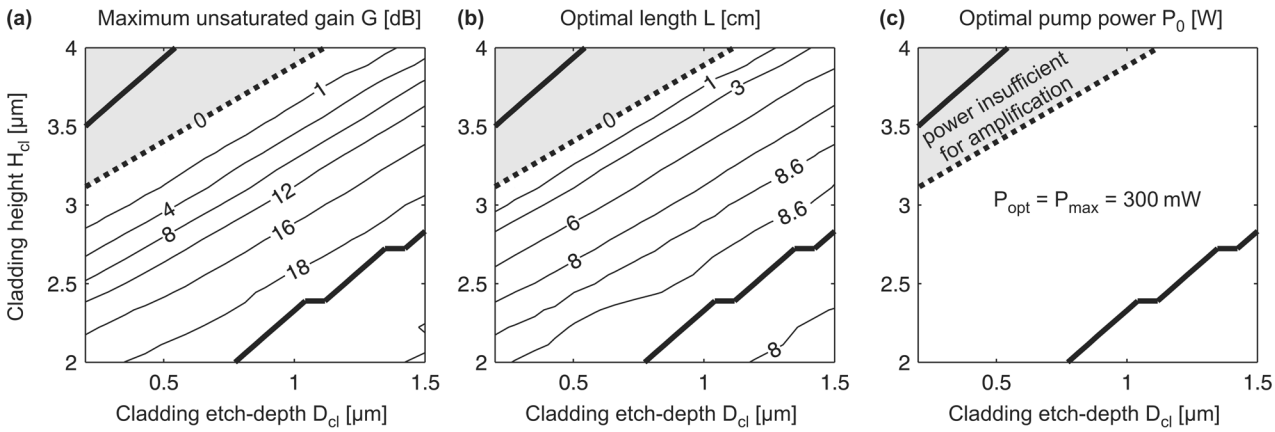

Fig. 5. For maximum available pump power of 300 mW: (a) maximum possible gain G of cladding-pumped silicon Raman amplifiers versus cladding height $H_{\rm cl}$ and etch depth $D_{\rm cl}$, and (b) the corresponding optimal lengths and (c) pump powers. If the pump power were injected directly into the silicon core, the maximum possible gain would be only 6.1 dB. The thick solid lines enclose the region where the structure guides only the two desired Stokes and pump modes shown in Fig. 2 and no higher order modes.

modes and thus undesired scattering-based interference effects are suppressed. Scattering of the pump mode with $n_{\rm eff} \approx 2.0$ to the close-lying radiation modes of the silica substrate ($n_{\rm eff} < 1.447$) will then be responsible for the biggest part of the total scattering losses α_p of the pump mode. As we show below, the technology has to be optimized such that these losses are low, otherwise the cladding-pumped amplifier has no advantage over direct core pumping (see Fig. 10). Therefore, if these losses are low enough, the even weaker coupling of the pump mode to the remote (in k space) fundamental mode will not impair the amplifier operation.

C. Gain for Practical Pump Powers

In Section III-A, we discussed the maximum possible gain of our cladding-pumped SRA for the case that the available pump power was unlimited. Fig. 3(a) shows that unsaturated gains exceeding 70 dB are possible with the chosen structure, but that the required pump powers would be more than 10 W, see Fig. 3(c). The question arises now what gains can be achieved with practical pump powers. To this aim, the thick solid curve in Fig. 4 shows the achievable gain as a function of the available pump power. In calculating this curve we have chosen a fixed cladding height of $H_{\rm cl} = 2.5$ μm, and we have optimized the amplifier length L as well as the cladding etch-depth $D_{\rm cl}$ [the latter only in the range between 0.2 and 1.2 μm, corresponding to the single-moded part of the horizontal axis in Fig. 3(a)]. Fig. 4 shows that even with pump powers as low as 200 mW, gains exceeding 10 dB can be achieved with a cladding-pumped SRA.

As another illustration, from now on we place an upper limit of 300 mW on the available pump power. This power limit is within the reach of cheap and compact laser diodes based on self-assembled In(Ga)As–GaAs quantum dots [39]. High-power quantum-dot lasers operating from 1.0 to 1.3 μm are commercially available [40]. Given this pump-power limit, Fig. 5(a) shows the maximum gains that are possible in our cladding-pumped SRA as a function of the cladding height $H_{\rm cl}$ and etch depth $D_{\rm cl}$, while Fig. 5(b) and (c) shows the corresponding optimal amplifier lengths and pump powers, respectively. It is seen that even with a pump-power limit of 300 mW, significant gains

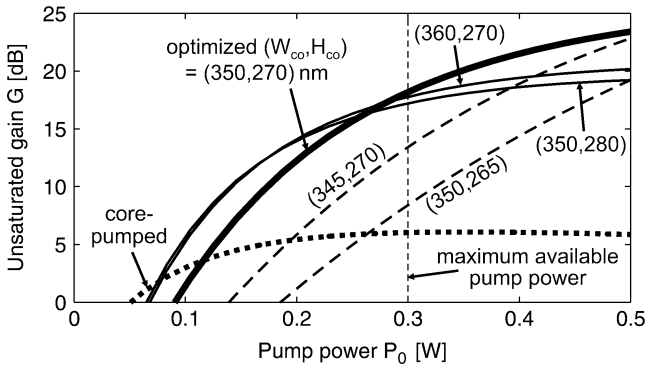

Fig. 6. Characteristics of a cladding-pumped silicon Raman amplifier optimized for a pump power of 300 mW (thick solid curve), and for SRAs with slight deviations in the silicon-core dimensions $W_{\rm co}$ and $H_{\rm co}$ (thin curves). The thick dotted curve shows the characteristics of the optimal core-pumped SRA.

of more than 18 dB can be achieved with the cladding-pumped SRA, while the core-pumped SRA could deliver only 6.1 dB, see Section III-A. However, for configurations above the thick dotted line in the upper left corner of Fig. 5, the pump power is not sufficient to achieve any positive gain, because the cladding is simply too large—the fraction of the pump power that overlaps with the silicon core is too low to produce enough Raman gain.

Finally, the thick solid curve in Fig. 6 shows the amplifier characteristics (unsaturated gain G versus pump power P_0) for one of the configurations of Fig. 5(a) with the maximum possible gain, namely for $H_{\rm cl} = 2.5$ μm and $D_{\rm cl} = 1.0$ μm, while the thick dotted curve in Fig. 6 shows the characteristics of the optimal core-pumped amplifier.

D. Principle Behind Gain Enhancement

As compared to the core-pumping concept, in cladding-pumped SRAs the effect of FCA on the pump power propagating in the amplifier is weakened by keeping it away from the silicon; only a small part of the pump mode extends into the silicon core [see Fig. 2(b)] and amplifies the Stokes mode through SRS. It also generates free carriers through TPA, as in a conventional core-pumped amplifier, and the resulting FCA will affect both the Stokes and the pump mode. However, the pump

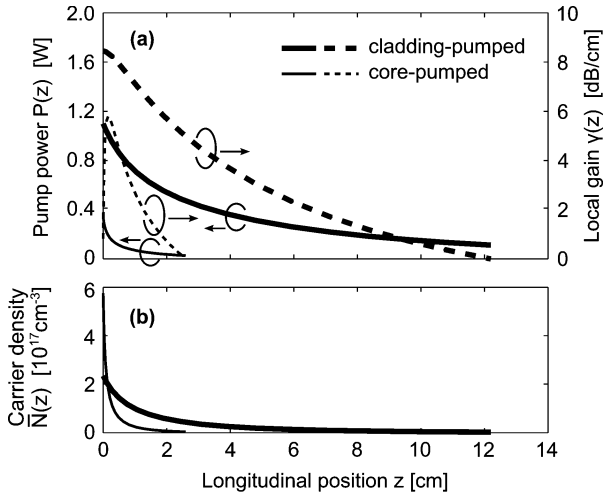

Fig. 7. (a) Longitudinal evolution of the pump power $P(z)$ (solid) and the corresponding local Stokes gain $\gamma(z)$ (dashed) in a cladding-pumped amplifier (thick) and the optimal core-pumped amplifier (thin). In the cladding-pumped amplifier, the pump power decays much slower due to pump-FCA mitigation; additionally the local Stokes gain can be larger than in the core-pumped amplifier. (b) Corresponding free-carrier density $\bar{N}$ according to (9).

mode is much less affected, because it is concentrated outside of the silicon and thus overlaps only slightly with the free carriers. If the cladding is large enough, the pump power can propagate without being significantly attenuated by FCA—the main effect limiting the efficiency of core-pumped amplifiers [14] has thus been reduced. Consequently, the amplifier can be longer than in the core-pumped case and deliver more gain.

However, the larger the cladding (i.e., the further the pump mode is extracted from the silicon), the more pump power must be injected in order to keep the pump intensity in the silicon core high enough to enable Raman amplification. Therefore, the practically available pump power will set an upper limit to the size of the cladding and thus to the amount of pump-FCA reduction. This is reflected in the optimization result shown in Fig. 4: for low available pump powers, the optimized cladding etch-depth D_{cl} (dashed-dotted) as well as the corresponding pump confinement factor η_p (dotted) are larger than for high available pump powers.

The solid curves in Fig. 7(a) illustrate the effect of pump-FCA mitigation. The thin solid curve shows the pump-power evolution along the waveguide for the optimal core-pumped amplifier: the pump power decays rapidly due to a strong overlap of the pump with the silicon core ($\eta_p = 1.0$) and the corresponding strong FCA. In contrast, the thick solid curve in Fig. 7 shows the pump-power evolution in the cladding-pumped amplifier optimized in Fig. 4 for a pump power of 1.1 W. Here, the pump power decays much more slowly, because the overlap of the pump mode with the silicon is now only $\eta_p = 0.20$. The cladding-pumped SRA can consequently be much longer than the core-pumped SRA, thus the total gain is higher. Note that the actual free-carrier density $\bar{N}$ inside the silicon core is comparable in the two cases, which is shown in Fig. 7(b).

Finally, in the considered cladding-pumped SRA the local Stokes gain is larger than in the core-pumped case. This effect is illustrated by the dashed curves in Fig. 7, which show the evolution of the local Stokes gain $\gamma(z)$ [defined in (2)] along the waveguide. While for the core-pumped amplifier [thin dashed curve in Fig. 7(a)], the local Stokes gain never exceeds 5.8 dB/cm, in the cladding-pumped amplifier (thick dashed curve) it can evidently be higher, namely 8.9 dB/cm here, which further contributes to the large total gain of the cladding-pumped SRA.

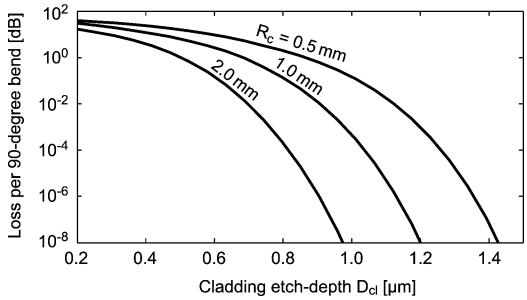

Fig. 8. Radiation losses of the cladding-pumping mode per 90-degree bend in the waveguide with cladding height $H_{\mathrm{cl}} = 2.5$ μm versus etch depth D_{cl} for three different radii of curvature R_c.

E. Bending Losses

As the optimal lengths of cladding-pumped SRAs may be on the order of tens of centimeters [see Fig. 3(b)], the waveguide shown in Fig. 1 will have to be at least partly curved to fit onto a silicon chip. It is, therefore, necessary to design the waveguide such that small curvature radii are tolerated without introducing too high losses. The losses in a waveguide bend consist of two contributions: the pure radiation loss which can be calculated from the imaginary part of the complex propagation constant of the leaky mode [37], and the loss that occurs at the transition from the straight to the curved waveguide.

Fig. 8 shows the pure radiation loss, calculated as in [37], of the cladding-pumping mode per 90-degree bend as a function of the cladding etch-depth D_{cl}, while the total cladding height has been kept fixed at $H_{\mathrm{cl}} = 2.5$ μm (as in Fig. 4). Fig. 8 shows that the bending loss decreases when etching the rib cladding further down, i.e., by increasing D_{cl}. However, an upper limit to the etch depth is given by the onset of additional undesired cladding modes at $D_{\mathrm{cl}} = 1.2$ μm (see Section III-B). For example, the waveguide corresponding to the cladding-pumped SRA whose characteristics are shown as the thick solid line in Fig. 6 ($D_{\mathrm{cl}} = 1.0$ μm) can be curved with radii down to 0.5 mm, where the bending loss still has an acceptable value of 0.15 dB per 90-degree bend. The transition losses, on the other hand, can be avoided by smoothly varying the radius of curvature along the propagation direction instead of having an abrupt transition from $R_c = \infty$ (straight waveguide) to the desired R_c. Finally, note that the fundamental mode of the entire structure, i.e., the Stokes mode, will have much lower curvature losses due to the higher index contrast between the silicon core and the surrounding materials, and thus the curvature loss of the cladding mode is the only limiting criterion to be considered.

IV. Fabrication Tolerances

We now consider the effects of deviations from the intended design of a cladding-pumped SRA. Figs. 3 and 5 show that changes of the rib-cladding dimensions on the order of 100 nm only relatively weakly influence the amplifier characteristics. On the other hand, the question remains what are the effects of deviations in the silicon-core dimensions.

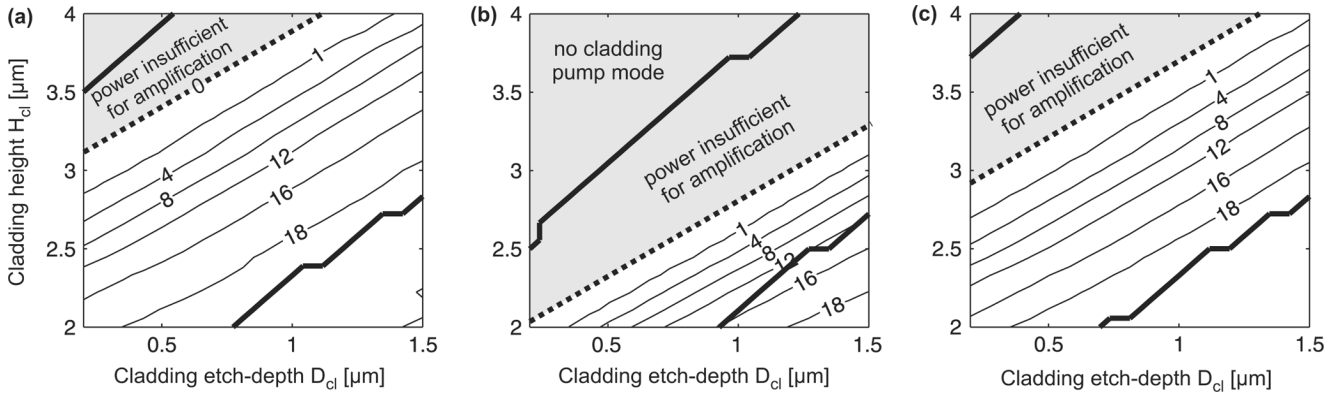

Fig. 9. Maximum possible gain of cladding-pumped amplifiers for a pump-power limit of 300 mW: (a) silicon-core dimensions as designed (350×270 nm^2, identical to Fig. 5(a)); (b) core too small ($W_{\rm co} = 340$ nm); (c) still $W_{\rm co} = 340$ nm, but pump wavelength decreased from 1220 to 1205 nm.

A. Deviations in Silicon-Core Dimensions

Consider again the thick solid curve in Fig. 6, which shows the amplifier characteristics for one of the configurations of Fig. 5(a) with the maximum possible gain, namely for $H_{\rm cl} = 2.5$ μm and $D_{\rm cl} = 1.0$ μm. At the maximum available pump power of 300 mW, Fig. 6 shows that this optimized amplifier delivers 18 dB gain. Its core dimensions are $W_{\rm co} = 350$ nm and $H_{\rm co} = 270$ nm, see the beginning of Section III. In contrast, the various thin curves in Fig. 6 show the characteristics of this amplifier for slight deviations from these silicon-core dimensions. For deviations as small as 5 nm, the amplifier gain at $P_0 = 300$ mW can drop down to 8 dB.

The origin of this strong dependence of the gain on the silicon-core dimensions lies in a spatial redistribution of the power inside the pump mode, which is very sensitive to the dimensions of the silicon core with its high refractive index. The thick solid curve in Fig. 6 shows the characteristics of the cladding-pumped SRA as designed. If the silicon core is accidentally made larger than designed (corresponding to the two thin solid curves in Fig. 6), the pump mode is "drawn" more into the silicon. The consequence is that on the one hand, Raman gain sets in at lower overall pump powers (the amplifier reaches its 0 dB threshold at lower pump powers), but on the other hand FCA has a stronger influence on the pump mode which reduces the possible overall gain at larger pump powers; both of these consequences can be seen in the two thin solid curves in Fig. 6. On the other hand, if the silicon core is made smaller than designed (dashed curves in Fig. 6), the pump power is released into the cladding. The reduced overlap of the pump mode with the silicon then requires larger pump powers to reach the threshold but permits larger total gains due to less influence of FCA on the pump mode. Only at the core dimensions $W_{\rm co} = 350$ nm and $H_{\rm co} = 270$ nm, corresponding to the thick solid curve in Fig. 6, is the fraction of pump power in the core optimal such that the amplifier gain at the pump power of 300 mW is maximal.

B. Changes in the Pump Wavelength

However, a similar spatial redistribution of the power inside the pump mode also takes place when the pump wavelength is changed [21]. Consider Fig. 9(a), which shows the maximum possible gain as a function of the cladding dimensions for the original core dimensions of $W_{\rm co} = 350$ nm and $H_{\rm co} = 270$ nm [Fig. 9(a) is identical to Fig. 5(a)]. If now the core were 10 nm too small, we would, after the discussion in Section IV-A, expect a significant change of those results. The gain for the new $W_{\rm co} = 340$ nm is shown in Fig. 9(b). The various contour lines for equal gain have shifted towards the lower right corner of the figure as compared to Fig. 9(a), as a consequence of the reduced confinement of the pump modes to the silicon core. If we now decrease the pump wavelength from 1220 to 1205 nm, the confinement of pump mode to the silicon will increase again. Indeed, the result shown in Fig. 9(c) shows that the contour lines have shifted back almost to their original position from Fig. 9(a). Not shown here are the optimal lengths and pump powers, which behave in a similar way.

In practice, this pump-wavelength dependence of the amplifier gain can be used to get an idea how the silicon-core size should be adjusted in order to achieve operation at the desired pump (and thus Stokes) wavelength. In case a given prototype has its largest gain at a pump wavelength shorter than the desired one, the core may be too small and thus should be larger in the new prototype (as in the example shown in Fig. 9). On the other hand, if the gain is largest at a pump wavelength that is too long, the new prototype should have a smaller core.

V. Gain Versus Linear and Non-Linear Losses

So far, all our simulations have been performed for fixed Stokes and cladding-mode losses of $\alpha_s = 2.0$ dB/cm and $\alpha_p = 0.5$ dB/cm, respectively, while the effective free-carrier lifetime has been assumed to be $\tau_{\rm eff} = 1$ ns.

To show that the cladding-pumped SRA performs much better than the core-pumped SRA in a wide range of these parameters, we show in Fig. 10 the maximum possible gain of the cladding-pumped SRA corresponding to the thick curves in Fig. 7, i.e., for cladding dimensions $H_{\rm cl} = 2.5$ μm and $D_{\rm cl} = 1.2$ μm. We have varied the linear pump and Stokes losses as well as the free-carrier lifetime, and for each parameter set we have optimized the amplifier length for a maximum pump power of 300 mW such that the total gain is maximized. Fig. 10 shows that the cladding-pumped SRAs (solid curves) can deliver significantly more gain than the core-pumped SRAs (dotted curves). Low linear losses α_p of the cladding-pumping mode are beneficial, because the total pump attenuation will be lower, the amplifier longer and the total gain higher. On

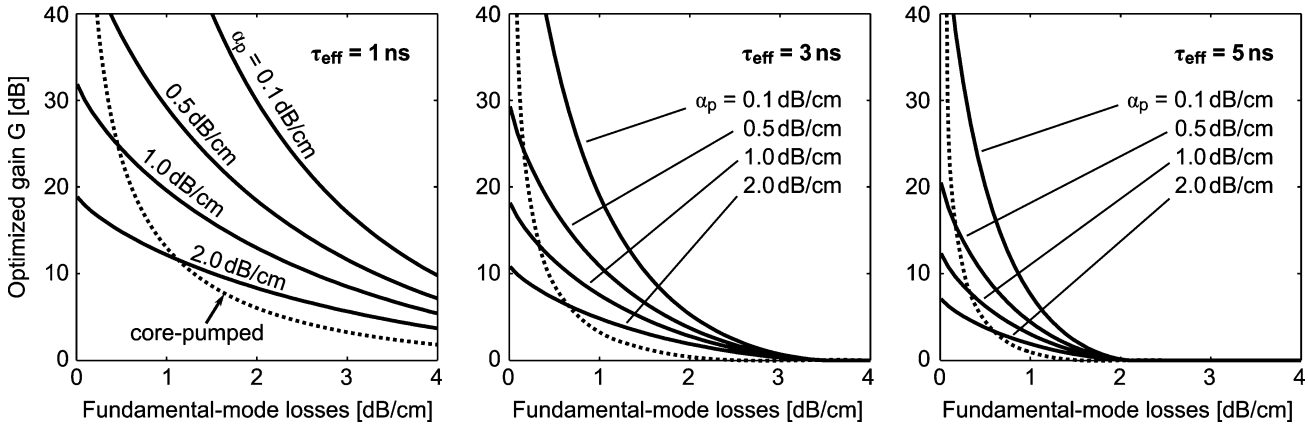

Fig. 10. Maximum possible gain of SRAs with cladding dimensions $W_{\rm cl} = 1.5\ \mu$m, $H_{\rm cl} = 2.5\ \mu$m and $D_{\rm cl} = 1.2\ \mu$m as a function of the fundamental-mode losses α_s for three different free-carrier lifetimes $\tau_{\rm eff}$, and maximum available pump power of 300 mW. The dotted curves show the maximum possible gain of core-pumped SRAs, while the solid curves correspond to cladding-pumped SRAs with varying pump-mode losses α_p.

the other hand, low linear Stokes losses α_s increase the local Stokes gain, thus contributing to a higher total gain. Finally, short lifetimes $\tau_{\rm eff}$ result in both decreased pump attenuation (longer amplifiers) and a larger local Stokes gain. Note that the gain of cladding-pumped SRAs could be optimized even more by adjusting the cladding and core dimensions, which we have kept fixed during the optimization for Fig. 10.

VI. Conclusion

We have shown in this paper that cladding-pumped silicon Raman amplifiers can deliver significantly more gain than conventional core-pumped amplifiers. We have presented a cladding-pumped design with an enhanced total gain of 18 dB that is achieved at a pump power of 300 mW. The idea behind the gain enhancement is that the pump power is guided mainly in the nonsilicon cladding with no free-carrier absorption. The reduced overlap of the pump mode with the silicon core weakens the effect of free-carrier absorption on the pump wave, thus permitting longer amplifiers with larger total gain.

Appendix A
Derivation of Effective Areas

In this appendix, we sketch how the expressions (3) and (5) for the effective areas describing SRS and TPA in a silicon waveguide have been derived [24].

A. Coupled-Mode Equations

Full-vectorial, nonlinear coupled-mode theory shows that the longitudinal evolution of co-propagating monochromatic pump and Stokes waves with powers P and S, respectively, is governed by the differential equations [23], [25], [41], [24]

$$\frac{1}{P}\frac{dP}{dz} = \Gamma_{\rm pp}P + 2\Gamma_{ps}S \tag{12}$$

$$\frac{1}{S}\frac{dS}{dz} = \Gamma_{\rm ss}S + 2\Gamma_{\rm sp}P \tag{13}$$

where

$$\Gamma_{ab} = \frac{3\epsilon_0\omega_a}{8\hat{N}_a\hat{N}_b}{\rm Im}\int_{\rm Si}\chi^{(3)}_{ijkl}(\omega_a,\omega_b,-\omega_b)e_a^{i*}e_a^j e_b^k e_b^{l*}\,dA \tag{14}$$

are the coefficients that describe the strength of the nonlinear effects. They depend on both the waveguide structure (through the Stokes and pump mode fields $\mathbf{e}_s$ and $\mathbf{e}_p$) and on the material properties (through the nonlinear susceptibility tensor $\chi^{(3)}$). We assume that only the silicon core has a significant nonlinearity, so that the integration in (14) extends only over the silicon part of the waveguide cross section. We use the Einstein sum convention, i.e., a summation of i, j, k, l over the coordinates x, y, z defined in Fig. 1 is implicit on the right-hand side of (14), ϵ_0 is the permittivity of free space, $\omega_{p,s}$ are the optical angular frequencies, and the remaining quantities have been defined in Section II.

The goal of this appendix is to introduce effective areas in terms of which (12) and (13) can be written in a form that is consistent with the usual notation in fiber optics [42]

$$\frac{1}{P}\frac{dP}{dz} = -\frac{\beta_{\rm pp}}{A^{(\rm TPA)}_{\rm pp}}P - \frac{\lambda_s}{\lambda_p}\left[\frac{g}{A^{(\rm SRS)}} + \frac{2\beta_{\rm sp}}{A^{(\rm TPA)}_{\rm sp}}\right]S \tag{15}$$

$$\frac{1}{S}\frac{dS}{dz} = -\frac{\beta_{\rm ss}}{A^{(\rm TPA)}_{\rm ss}}S + \left[\frac{g}{A^{(\rm SRS)}} - \frac{2\beta_{\rm sp}}{A^{(\rm TPA)}_{\rm sp}}\right]P \tag{16}$$

where the contribution of the pure nonlinear material has been extracted into the bulk TPA and SRS coefficients β_{ij} and g, and the information about the influence of the guiding geometry resides in the effective areas $A^{(\rm TPA)}_{ij}$ and $A^{(\rm SRS)}$.

B. General Form of Nonlinear Coefficients in Silicon

As pointed out in Section II-C, our waveguide is not oriented along the crystallographic axes of the silicon, but along a [011]-like direction. The following discussion is more convenient when we express the tensor-field product under the integral in (14) in a coordinate system coinciding with the crystallographic axes. We, therefore, write

$$\Gamma_{ab} = \frac{3\epsilon_0\omega_a}{8\hat{N}_a\hat{N}_b}\int_{\rm Si}{\rm Im}\left[\tilde{\chi}^{(3)}_{ijkl}(\omega_a,\omega_b,-\omega_b)\tilde{e}_a^{i*}\tilde{e}_a^j\tilde{e}_b^k\tilde{e}_b^{l*}\right]dA \tag{17}$$

where $\tilde{\chi}^{(3)}$ is the nonlinear susceptibility tensor with respect to the crystallographic axes, and the mode fields with respect to the latter are given by

$$\tilde{\mathbf{e}}_{p,s} = \mathbf{S}\mathbf{e}_{p,s} \tag{18}$$

where

$$\mathbf{S} = \frac{1}{\sqrt{2}} \begin{pmatrix} \sqrt{2} & 0 & 0 \\ 0 & 1 & 1 \\ 0 & -1 & 1 \end{pmatrix} \tag{19}$$

is the rotation matrix whose columns represent the unit vectors along the x, y, and z directions with respect to the crystallographic axes $\tilde{x}$, $\tilde{y}$, $\tilde{z}$.

As silicon is a cubic material belonging to the m3m class, all 81 components of the nonlinear susceptibility tensor $\tilde{\chi}^{(3)}(\omega_a, \omega_b, -\omega_b)$ can be fully expressed in terms of the four elements $\tilde{\chi}^{(3)}_{\tilde{x}\tilde{x}\tilde{x}\tilde{x}}$, $\tilde{\chi}^{(3)}_{\tilde{x}\tilde{x}\tilde{y}\tilde{y}}$, $\tilde{\chi}^{(3)}_{\tilde{x}\tilde{y}\tilde{x}\tilde{y}}$ and $\tilde{\chi}^{(3)}_{\tilde{x}\tilde{y}\tilde{y}\tilde{x}}$ as [26]

$$\begin{aligned}\tilde{\chi}^{(3)}_{ijkl} = {} & \tilde{\chi}^{(3)}_{\tilde{x}\tilde{x}\tilde{y}\tilde{y}}\delta_{ij}\delta_{kl} + \tilde{\chi}^{(3)}_{\tilde{x}\tilde{y}\tilde{x}\tilde{y}}\delta_{ik}\delta_{jl} \\ & + \tilde{\chi}^{(3)}_{\tilde{x}\tilde{y}\tilde{y}\tilde{x}}\delta_{il}\delta_{jk} + \tilde{\chi}^{(3)}_{\text{aniso}}\delta_{ijkl}\end{aligned} \tag{20}$$

where the frequency dependence $(\omega_a, \omega_b, -\omega_b)$ is implicitly assumed, we have defined $\tilde{\chi}^{(3)}_{\text{aniso}} = \tilde{\chi}^{(3)}_{\tilde{x}\tilde{x}\tilde{x}\tilde{x}} - \tilde{\chi}^{(3)}_{\tilde{x}\tilde{x}\tilde{y}\tilde{y}} - \tilde{\chi}^{(3)}_{\tilde{x}\tilde{y}\tilde{x}\tilde{y}} - \tilde{\chi}^{(3)}_{\tilde{x}\tilde{y}\tilde{y}\tilde{x}}$, and δ is the Kronecker symbol which is unity only when all of its indexes are equal. Using (20), we can evaluate the tensor-field product under the integral in (17), casting it in the form

$$\begin{aligned}\Gamma_{ab} = {} & \frac{3\epsilon_0\omega_a}{8\hat{N}_a\hat{N}_b}\int_{\text{Si}} \left[\text{Im}\tilde{\chi}^{(3)}_{\tilde{x}\tilde{x}\tilde{y}\tilde{y}}(\omega_a, \omega_b, -\omega_b)\right] |\mathbf{e}_a|^2|\mathbf{e}_b|^2 \\ & + \left[\text{Im}\tilde{\chi}^{(3)}_{\tilde{x}\tilde{y}\tilde{y}\tilde{x}}(\omega_a, \omega_b, -\omega_b)\right] |\mathbf{e}_a \cdot \mathbf{e}_b|^2 \\ & + \left[\text{Im}\tilde{\chi}^{(3)}_{\tilde{x}\tilde{y}\tilde{x}\tilde{y}}(\omega_a, \omega_b, -\omega_b)\right] |\mathbf{e}_a \cdot \mathbf{e}_b^*|^2 \\ & + \left[\text{Im}\tilde{\chi}^{(3)}_{\text{aniso}}(\omega_a, \omega_b, -\omega_b)\right] \sum_{i=\tilde{x},\tilde{y},\tilde{z}} |\tilde{e}_a^i|^2|\tilde{e}_b^i|^2 \, dA.\end{aligned} \tag{21}$$

In (21), the first three terms contain only dot products of the fields. As these remain unchanged by a rotation of the coordinate system, we can keep the fields in the original waveguide coordinates. Only in the last (anisotropic) contribution, the rotated fields from (18) have to be used.

C. Two-Photon Absorption (TPA)

One contribution to the imaginary part of the nonlinear susceptibilities occurring in (21) is due to TPA. Here, we assume that the four elements sufficient to specify the full $\chi^{(3)}$ tensor according to (20) have the form

$$\begin{aligned}\text{Im}\tilde{\chi}^{(3),\text{TPA}}_{\tilde{x}\tilde{x}\tilde{y}\tilde{y}}(\omega_a, \omega_b, -\omega_b) = {} & \text{Im}\tilde{\chi}^{(3),\text{TPA}}_{\tilde{x}\tilde{y}\tilde{x}\tilde{y}}(\omega_a, \omega_b, -\omega_b) \\ = {} & \text{Im}\tilde{\chi}^{(3),\text{TPA}}_{\tilde{x}\tilde{y}\tilde{y}\tilde{x}}(\omega_a, \omega_b, -\omega_b) \\ = {} & \frac{1}{3}C^{(\text{TPA})}(\omega_a, \omega_b)\end{aligned} \tag{22}$$

$$\text{Im}\tilde{\chi}^{(3),\text{TPA}}_{\text{aniso}}(\omega_a, \omega_b, -\omega_b) = 0. \tag{23}$$

The assumption expressed by (22) and (23) is that TPA in silicon is isotropic and that the Kleinman symmetry condition is valid [26]. On the one hand, this would mean that degenerate TPA (i.e., $\omega_a = \omega_b$) in silicon is isotropic with an incremental dichroism parameter [43] of $\delta = 1/3$. This is consistent with the experimental results available in the 1.55-μm region from [44], [45], [35], although other authors have recently reported a nonzero anisotropy [46]. On the other hand, as far as nondegenerate TPA (i.e., $\omega_a \neq \omega_b$) is concerned, we assume isotropicity and Kleinman symmetry even though no data is available in the literature to the best of the authors' knowledge.

Using (22) and (23), the TPA contribution to the nonlinear coefficient Γ_{ab} from (21) can be written

$$\begin{aligned}\Gamma^{(\text{TPA})}_{ab} = {} & \frac{\epsilon_0\omega_a C^{(\text{TPA})}(\omega_a, \omega_b)}{8\hat{N}_a\hat{N}_b}\int_{\text{Si}} |\mathbf{e}_a|^2|\mathbf{e}_b|^2 + |\mathbf{e}_a \cdot \mathbf{e}_b|^2 \\ & + |\mathbf{e}_a \cdot \mathbf{e}_b^*|^2 \, dA\end{aligned} \tag{24}$$

which we now want to express in the form in which it occurs in (15)–(16):

$$\Gamma^{(\text{TPA})}_{ab} = -\frac{\beta_{ab}}{A^{(\text{TPA})}_{ab}}. \tag{25}$$

In (25), the bulk TPA coefficient β_{ab} is a material constant describing the strength of TPA for homogeneous plane waves in silicon [47], and the effective area $A^{(\text{TPA})}_{ab}$ to be derived describes the influence of the waveguide geometry in terms of a compact formula involving only the mode fields and the waveguide shape. The bulk TPA coefficient is often specified for the case of waves linearly polarized along the same direction; it is then related to the nonlinear susceptibility tensor as [47]

$$\begin{aligned}\beta_{ab} = {} & -\frac{3\mu_0\omega_a}{2n_a n_b}\text{Im}\tilde{\chi}^{(3),\text{TPA}}_{\tilde{x}\tilde{x}\tilde{x}\tilde{x}}(\omega_a, \omega_b, -\omega_b) \\ = {} & -\frac{3\mu_0\omega_a}{2n_a n_b}C^{(\text{TPA})}(\omega_a, \omega_b)\end{aligned} \tag{26}$$

where μ_0 is the permeability of vacuum, and the second equality follows from (22) and (23). Solving (24)–(26) for $A^{(\text{TPA})}_{ab}$ yields the desired expression

$$\begin{aligned}A^{(\text{TPA})}_{ab} = {} & \frac{4Z_0^2\hat{N}_a\hat{N}_b}{n_a n_b}\left\{\frac{1}{3}\int_{\text{Si}} |\mathbf{e}_a|^2|\mathbf{e}_b|^2 + |\mathbf{e}_a \cdot \mathbf{e}_b|^2 \right. \\ & \left. + |\mathbf{e}_a \cdot \mathbf{e}_b^*|^2 \, dA\right\}^{-1}.\end{aligned} \tag{27}$$

Finally, it is clear from (27) that $A^{(\text{TPA})}_{ps} = A^{(\text{TPA})}_{\text{sp}}$. Since furthermore $\beta_{ps} = (\lambda_s/\lambda_p)\beta_{\text{sp}}$ [47], (25) shows that $\Gamma^{(\text{TPA})}_{ps} = (\lambda_s/\lambda_p)\Gamma^{(\text{TPA})}_{\text{sp}}$. Therefore, the contribution of nondegenerate TPA to the differential equation for the pump power [last term in (15)] is the same as that in the equation for the Stokes power, (16), multiplied by the ratio of the Stokes and pump wavelengths, λ_s/λ_p.

D. Stimulated Raman Scattering (SRS)

The second contribution to the imaginary part of the nonlinear susceptibilities occurring in (21) is that of SRS. Here, the four elements sufficient to specify the full $\chi^{(3)}$ tensor according to (20) are [25], [8]

$$\text{Im}\tilde{\chi}^{(3),\text{SRS}}_{\tilde{x}\tilde{x}\tilde{x}\tilde{x}}(\omega_s, \omega_p, -\omega_p) = 0 \tag{28}$$

$$\text{Im}\tilde{\chi}^{(3),\text{SRS}}_{\tilde{x}\tilde{x}\tilde{y}\tilde{y}}(\omega_s, \omega_p, -\omega_p) = C^{(\text{SRS})}(\omega_s, \omega_p) \tag{29}$$

$$\text{Im}\tilde{\chi}^{(3),\text{SRS}}_{\tilde{x}\tilde{y}\tilde{x}\tilde{y}}(\omega_s, \omega_p, -\omega_p) = 0 \tag{30}$$

$$\text{Im}\tilde{\chi}^{(3),\text{SRS}}_{\tilde{x}\tilde{y}\tilde{y}\tilde{x}}(\omega_s, \omega_p, -\omega_p) = C^{(\text{SRS})}(\omega_s, \omega_p) \tag{31}$$

such that $\text{Im}\tilde{\chi}^{(3),\text{SRS}}_{\text{aniso}}(\omega_s, \omega_p, -\omega_p) = -2C^{(\text{SRS})}(\omega_s, \omega_p)$. Inserting this into (21), and simplifying the resulting expression

by making use of the convention that the transverse (x, y) field components are real, while the z components are imaginary, we find that the nonlinear coefficient describing SRS is given by

$$\begin{aligned}\Gamma_{\rm sp}^{(\rm SRS)} = &\frac{3\epsilon_0\omega_s C^{(\rm SRS)}(\omega_s,\omega_p)}{8\hat{N}_s\hat{N}_p}\\ &\times\int_{\rm Si}|\mathbf{e}_s|^2|\mathbf{e}_p|^2+|\mathbf{e}_s\cdot\mathbf{e}_p|^2\\ &-2\left(e_s^x\right)^2\left(e_p^x\right)^2-\left[\left(e_s^y\right)^2-\left(e_s^z\right)^2\right]\\ &\cdot\left[\left(e_p^y\right)^2-\left(e_p^z\right)^2\right]dA. \end{aligned}\tag{32}$$

We now write the preceding result $\Gamma_{\rm sp}^{(\rm SRS)}$ in the form

$$2\Gamma_{\rm sp}^{(\rm SRS)} = \frac{g}{A^{(\rm SRS)}}\tag{33}$$

where the Raman-gain constant g describes the strength of SRS for homogeneous plane waves in the bulk material, and the effective area $A^{(\rm SRS)}$ to be derived describes the influence of the waveguide geometry. The bulk Raman-gain constant g in silicon is usually specified for linear Stokes and pump polarizations along orthogonal crystallographic axes [25], [8]. It is then related to the $\tilde{\chi}^{(3)}$ tensor given by (28)–(31) through [47]

$$\begin{aligned}g &= \frac{3\mu_0\omega_s}{n_s n_p}\mathrm{Im}\tilde{\chi}_{\tilde{x}\tilde{x}\tilde{y}\tilde{y}}^{(3),\rm SRS}(\omega_s,\omega_p,-\omega_p)\\ &= \frac{3\mu_0\omega_s}{n_s n_p}C^{(\rm SRS)}(\omega_s,\omega_p).\end{aligned}\tag{34}$$

Solving (32)–(34) for $A^{(\rm SRS)}$ gives the desired expression

$$\begin{aligned}A^{(\rm SRS)} = &\frac{4Z_0^2\hat{N}_p\hat{N}_s}{n_p n_s}\left\{\int_{\rm Si}|\mathbf{e}_p|^2|\mathbf{e}_s|^2+|\mathbf{e}_p\cdot\mathbf{e}_s|^2\right.\\ &-2\left(e_s^x\right)^2\left(e_p^x\right)^2-\left[\left(e_s^y\right)^2-\left(e_s^z\right)^2\right]\\ &\left.\cdot\left[\left(e_p^y\right)^2-\left(e_p^z\right)^2\right]dA\right\}^{-1}.\end{aligned}\tag{35}$$

Finally, using the symmetry property $\tilde{\chi}^{(3),\rm SRS}(\omega_p,\omega_s,-\omega_s) = \tilde{\chi}^{(3),\rm SRS}(\omega_s,\omega_p,-\omega_p)^*$ [47] in (21) shows that $\Gamma_{ps}^{(\rm SRS)} = -(\lambda_s/\lambda_p)\Gamma_{\rm sp}^{(\rm SRS)}$. Therefore, the SRS contributions to (15) and (16) are identical apart from a factor of $-\lambda_s/\lambda_p$.

The area $A^{(\rm SRS)}$ such derived is "effective" in the sense that a homogeneous pump plane wave propagating in bulk silicon must have the intensity $I_p = P/A^{(\rm SRS)}$ in order to amplify a co-propagating Stokes plane wave with a local Raman gain that is exactly as large as the gain provided by the pump power P to the Stokes power in a waveguide with the SRS effective area $A^{(\rm SRS)}$.

For weakly guiding waveguides and y-polarized mode fields, the effective areas derived in this appendix for TPA and SRS become identical and reduce to the one used in fiber optics [42]. However, in structures with high refractive-index contrast, such as the ones analyzed in the present paper, the effective areas for TPA and SRS may differ significantly. For example, for the optimized design shown in Fig. 6, the pump-Stokes-TPA effective area is $A_{\rm sp}^{(\rm TPA)} = 0.41\ \mu\mathrm{m}^2$, while the SRS effective area is only $A^{(\rm SRS)} = 0.23\ \mu\mathrm{m}^2$.

Appendix B
Relation Between M and the Effective Free-Carrier Lifetime $\tau_{\rm eff}$

In Section II-E, we have introduced the constant M that relates the total carrier-generation rate at the waveguide position z to the free-carrier density $\bar{N}$ in the steady state, thus characterizing the strength of FCA.

On the one hand, the constant M can be calculated when the recombination velocities at the silicon boundaries are known. From (6)–(8), we get [29]

$$M = \frac{\bar{N}}{G_{\rm tot}} = \left[\frac{A}{\tau_b}+\oint S(l)\,dl\right]^{-1}\tag{36}$$

where $A = W_{\rm co}\times H_{\rm co}$ is the silicon cross-sectional area, and the integral is over the entire boundary of the silicon core. If the recombination velocity at the interfaces to the media surrounding the silicon were constant $[S(l) = S_0 = \mathrm{const}]$, we would simply have

$$M = \frac{1}{A/\tau_b + 2(W_{\rm co}+H_{\rm co})S_0}\tag{37}$$

which is a special case of [29, eq. (4)] for equal interface and surface recombination velocities and zero rib height.

On the other hand, the constant M can be related to the effective free-carrier lifetime $\tau_{\rm eff}$ that is usually used in the literature to characterize FCA in waveguides [13], [38]. The relation between the two quantities can be derived by considering the situation where only one wave is propagating inside the waveguide. Dropping the respective subscripts p or s, in our model the power P evolves inside the waveguide according to

$$\frac{1}{I}\frac{dI}{dz} = -\alpha-\beta I-\frac{\eta\bar{\varphi}\lambda^2\beta M A^{(\rm TPA)}}{2h\nu}I^2\tag{38}$$

where $I = P/A^{(\rm TPA)}$ is an effective intensity. On the other hand, in conventional models of SRAs [13], [5], [8] the evolution of an effective intensity I' is described by

$$\frac{1}{I'}\frac{dI'}{dz} = -\alpha-\beta I'-\frac{\bar{\varphi}\lambda^2\beta\tau_{\rm eff}}{2h\nu}I'^2.\tag{39}$$

We now require that our model (38) and the conventional model (39) both predict the same longitudinal evolution of the effective intensity along the waveguide. Then we must have

$$\tau_{\rm eff} = \eta A^{(\rm TPA)}M\tag{40}$$

which is the desired result.

Equation (40) shows that the effective free-carrier lifetime $\tau_{\rm eff}$ depends on the considered mode of the waveguide. Different modes will thus "see" different effective lifetimes. On the other hand, in our formulation there is only one parameter M describing the carrier-diffusion process (see Section II-E), and the extent to which each individual mode contributes to carrier generation is represented by the effective areas in (9), while the extent to which each individual mode is influenced by FCA is represented in (1)–(2) by the confinement factors (10).

Using (40), we obtain the M required for our simulations as follows: for a waveguide of the dimensions considered in this paper ($350\times 270\ \mathrm{nm}^2$, see Section III), a typical lifetime

seen by the fundamental mode would be $\tau_{\text{eff}} = 1$ ns [38]. The effective area and the confinement factor of the fundamental mode are calculated at our wavelength of 1220 nm to be $A^{(\text{TPA})} = 0.082\ \mu\text{m}^2$ and $\eta = 1.0$, respectively, yielding an M of 1.2×10^4 s/m^2.

REFERENCES

[1] R. Soref, "The past, present, and future of silicon photonics," *IEEE J. Sel. Topics Quantum Electron.*, vol. 12, no. 6, pp. 1678–1687, Nov./Dec. 2006.

[2] B. Jalali, "Teaching silicon new tricks," *Nature Photon.*, vol. 1, pp. 193–195, 2007.

[3] R. Claps, D. Dimitropoulos, V. Raghunathan, Y. Han, and B. Jalali, "Observation of stimulated Raman amplification in silicon waveguides," *Opt. Exp.*, vol. 11, no. 15, pp. 1731–1739, Jul. 2003.

[4] R. L. Espinola, J. I. Dadap, J. Richard, M. Osgood, S. J. McNab, and Y. A. Vlasov, "Raman amplification in ultrasmall silicon-on-insulator wire waveguides," *Opt. Exp.*, vol. 12, no. 16, pp. 3713–3718, Aug. 2004.

[5] H. Rong, A. Liu, R. Nicolaescu, M. Paniccia, O. Cohen, and D. Hak, "Raman gain and nonlinear optical absorption measurement in a low-loss silicon waveguide," *Appl. Phys. Lett.*, vol. 85, no. 12, pp. 2196–2198, Sep. 2004.

[6] Q. Xu, V. R. Almeida, and M. Lipson, "Demonstration of high Raman gain in a submicrometer-size silicon-on-insulator waveguide," *Opt. Lett.*, vol. 30, no. 1, pp. 35–37, Jan. 2005.

[7] V. Raghunathan, O. Boyraz, and B. Jalali, "20 dB on-off Raman amplification in silicon waveguides," presented at the Conf. Lasers Electro-Optics (CLEO), 2005, paper CMU1.

[8] A. Liu, H. Rong, R. Jones, O. Cohen, D. Hak, and M. Paniccia, "Optical amplification and lasing by stimulated Raman scattering in silicon waveguides," *J. Lightw. Technol.*, vol. 24, no. 3, pp. 1440–1455, Mar. 2006.

[9] O. Boyraz and B. Jalali, "Demonstration of a silicon Raman laser," *Opt. Exp.*, vol. 12, no. 21, pp. 5269–5273, Oct. 2004.

[10] H. Rong, S. Xu, Y.-H. Kuo, V. Sih, O. Cohen, O. Raday, and M. Paniccia, "Low-threshold continuous-wave Raman silicon laser," *Nature Photon.*, 2007.

[11] B. Jalali, V. Raghunathan, D. Dimitropoulos, and Ö. Boyraz, "Raman-based silicon photonics," *IEEE J. Sel. Top. Quantum Electron.*, vol. 12, no. 3, pp. 412–421, May/Jun. 2006.

[12] D. R. Zimmerman and L. H. Spiekman, "Amplifiers for the masses: EDFA, EDWA, and SOA amplets for metro and access applications," *J. Lightw. Technol.*, vol. 22, no. 1, pp. 63–70, Jan. 2004.

[13] R. Claps, V. Raghunathan, D. Dimitropoulos, and B. Jalali, "Influence of nonlinear absorption on Raman amplification in Silicon waveguides," *Opt. Exp.*, vol. 12, no. 12, pp. 2774–2780, Jun. 2004.

[14] H. Renner and M. Krause, "Maximal total gain of nontapered silicon-on-insulator Raman amplifiers," presented at the Opt. Amp. Their Applications (OAA) Topical Meeting, 2006, Paper OMD2.

[15] Y. Liu and H. K. Tsang, "Nonlinear absorption and Raman gain in helium-ion-implanted silicon waveguides," *Opt. Lett.*, vol. 31, no. 11, pp. 1714–1716, Jun. 2006.

[16] T. Tanabe, K. Nishiguchi, A. Shinya, E. Kuramochi, H. Inokawa, M. Notomi, K. Yamada, T. Tsuchizawa, T. Watanabe, H. Fukuda, H. Shinojima, and S. Itabashi, "Fast all-optical switching using ion-implanted silicon photonic crystal nanocavities," *Appl. Phys. Lett.*, vol. 90, p. 031115, Jan. 2007.

[17] M. Först, J. Niehusmann, T. Plötzing, J. Bolten, T. Wahlbrink, C. Moormann, and H. Kurz, "High-speed all-optical switching in ion-implanted silicon-on-insulator microring resonators," *Opt. Lett.*, vol. 32, no. 14, pp. 2046–2048, Jul. 2007.

[18] S. Fathpour, K. K. Tsia, and B. Jalali, "Energy harvesting in silicon Raman amplifiers," *Appl. Phys. Lett.*, vol. 89, p. 061109, Aug. 2006.

[19] D. Dimitropoulos, S. Fathpour, and B. Jalali, "Limitations of active carrier removal in silicon Raman amplifiers and lasers," *Appl. Phys. Lett.*, vol. 87, p. 261108, 2005.

[20] H. Renner, M. Krause, and E. Brinkmeyer, "Maximal gain and optimal taper design for Raman amplifiers in silicon-on-insulator waveguides," presented at the Integrated Photonics Research and Applications Topical Meeting (IPRA), 2005, Paper JWA3.

[21] M. Krause, H. Renner, E. Brinkmeyer, S. Fathpour, D. Dimitropoulos, V. Raghunathan, and B. Jalali, "Efficient Raman amplification in cladding-pumped silicon waveguides," presented at the 3rd Int. Conference on Group IV Photonics (GFP), 2006, paper P6.

[22] G.-L. Bona, R. Germann, and B. J. Offrein, "SiON high-refractive-index waveguide and planar lightwave circuits," *IBM J. Res. & Dev.*, vol. 47, no. 2/3, pp. 239–249, Mar./May 2003.

[23] J. E. Sipe, C. M. de Sterke, and B. J. Eggleton, "Rigorous derivation of coupled mode equations for short, high-intensity grating-coupled, co-propagating pulses," *J. Mod. Opt.*, vol. 49, no. 9, pp. 1437–1452, 2002.

[24] M. Krause, "Efficient Raman amplifiers and lasers in optical fibers and silicon waveguides: New concepts," Ph.D. dissertation, Technische Universität Hamburg-Harburg, Hamburg, Germany, 2007.

[25] D. Dimitropoulos, B. Houshmand, R. Claps, and B. Jalali, "Coupled-mode theory of the Raman effect in silicon-on-insulator waveguides," *Opt. Lett.*, vol. 28, no. 20, pp. 1954–1956, Oct. 2003.

[26] R. W. Boyd, *Nonlinear Optics*, 2nd ed. New York: Academic, 2003.

[27] J. P. McKelvey, *Solid State and Semiconductor Physics*. New York: Harper & Row, 1966.

[28] K. Seeger, *Semiconductor Physics*, 5th ed. New York: Springer-Verlag, 1991.

[29] D. Dimitropoulos, R. Jhaveri, R. Claps, J. C. S. Woo, and B. Jalali, "Lifetime of photogenerated carriers in silicon-on-insulator rib waveguides," *Appl. Phys. Lett.*, vol. 86, p. 071115, 2005.

[30] A. W. Snyder and J. D. Love, *Optical Waveguide Theory*. New York: Chapman and Hall, 1983.

[31] I. H. Malitson, "Interspecimen comparison of the refractive index of fused silica," *J. Opt. Soc. Amer.*, vol. 55, no. 10, pp. 1205–1209, Oct. 1965.

[32] H. H. Li, "Refractive index of silicon and germanium and its wavelength and temperature derivatives," *J. Phys. Chem. Ref. Data*, vol. 9, no. 3, pp. 561–658, Jul. 1980.

[33] M. Dinu, "Dispersion of phononassisted nonresonant third-order nonlinearities," *IEEE J. Quantum Electron.*, vol. 39, no. 11, pp. 1498–1503, Nov. 2003.

[34] Q. Lin, J. Zhang, G. Piredda, R. W. Boyd, P. M. Fauchet, and G. P. Agrawal, "Dispersion of silicon nonlinearities in the near infrared region," *Appl. Phys. Lett.*, p. 021111, 2007.

[35] A. D. Bristow, N. Rotenberg, and H. M. van Driel, "Two-photon absorption and Kerr coefficients of silicon for 850-2200 nm," *Appl. Phys. Lett.*, vol. 90, p. 191104, 2007.

[36] M. Krause, R. Draheim, H. Renner, and E. Brinkmeyer, "Cascaded silicon Raman lasers as mid-infrared sources," *Electron. Lett.*, vol. 42, no. 21, pp. 1224–1226, Oct. 2006.

[37] M. Krause, H. Renner, and E. Brinkmeyer, "Polarization-dependent curvature loss in silicon rib waveguides," *IEEE J. Sel. Top. Quantum Electron.*, vol. 12, no. 6, pp. 1359–1362, Nov./Dec. 2006.

[38] H. Yamada, M. Shirane, T. Chu, H. Yokoyama, S. Ishida, and Y. Arakawa, "Nonlinear-optic silicon-nanowire waveguides," *Jpn. J. Appl. Phys.*, vol. 44, pp. 6541–6545, 2005.

[39] M. V. Maximov, Y. M. Shernyakov, A. F. Tsatsul'nikov, A. V. Lunev, A. V. Sakharov, V. M. Ustinov, A. Y. Egorov, A. E. Zhukov, A. R. Kovsh, P. S. Kop'ev, L. V. Asryan, Z. I. Alferov, N. N. Ledentsov, D. Bimberg, A. O. Kosogov, and P. Werner, "High-power continuous-wave operation of a InGaAs/AlGaAs quantum dot laser," *J. Appl. Phys.*, vol. 83, no. 10, pp. 5561–5563, May 1998.

[40] Innolume Inc. Products. Santa C lara, CA [Online]. Available: http://www.innolume.com/, 2007

[41] X. Chen, N. C. Panoiu, and R. M. Osgood Jr., "Theory of Raman-mediated pulsed amplification in silicon-wire waveguides," *IEEE J. Quantum Electron.*, vol. 42, no. 2, pp. 160–170, Feb. 2006.

[42] G. P. Agrawal, *Nonlinear Fiber Optics*, 3rd ed. New York: Academic, 2001.

[43] D. C. Hutchings and B. S. Wherrett, "Theory of anisotropy of two-photon absorption in zinc-blende semiconductors," *Phys. Rev. B*, vol. 49, no. 4, pp. 2418–2426, Jan. 1994.

[44] M. Dinu, F. Quochi, and H. Garcia, "Third-order nonlinearities in silicon at telecom wavelengths," *Appl. Phys. Lett.*, vol. 82, no. 18, pp. 2954–2956, May 2003.

[45] R. Salem and T. E. Murphy, "Polarization-insensitive cross correlation using two-photon absorption in a silicon photodiode," *Opt. Lett.*, vol. 29, no. 13, pp. 1524–1526, Jul. 2004.

[46] Q. Lin, J. Zhang, G. Piredda, R. W. Boyd, P. M. Fauchet, and G. P. Agrawal, "Anisotropic nonlinear response of silicon in the near-infrared region," presented at the Conf. Lasers and Electro-Optics (CLEO), 2007, Paper CMHH3.

[47] Y.-R. Shen, *The Principles of Nonlinear Optics*. New York: Wiley, 1984.

Michael Krause received the Dipl.-Ing. and Dr.-Ing. degrees in electrical engineering from the Technische Universität Hamburg-Harburg (TUHH), Hamburg, Germany, in 2003 and 2007, respectively.

He is currently a Postdoctoral Researcher in the Department of Optical Communication Technology, TUHH, doing research on the modeling and design of linear and nonlinear silicon-photonics components. His research interests include Raman amplification and lasing in optical fibers and silicon waveguides, numerical methods for guided-wave optics, and general waveguide theory.

Hagen Renner received the Dipl.-Ing. and Dr.-Ing. degrees from the Technical University of Dresden, Dresden, Germany, in 1985 and 1990, respectively, both in electrical engineering.

Since 1991, he has been with the Technische Universität Hamburg-Harburg, Hamburg, Germany, where he is currently a Senior Engineer in the Optical Communication Technology group. His current research interests include fiber and integrated optics, waveguide design, Bragg gratings, and Raman scattering in fibers and silicon waveguides.

Sasan Fathpour received the B.S. and M.A.Sc. degrees in electrical engineering from Isfahan University of Technology, Iran, in 1995 and the University of British Columbia (UBC), BC, Canada, in 2000, respectively. He received the Ph.D. degree in electrical engineering from the University of Michigan, Ann Arbor, in 2005. His Ph.D. dissertation was on epitaxial growth, fabrication, characterization and modeling of In(Ga)As self-assembled quantum dot lasers, with record high dynamic and static performances, as well as on spin-polarized light sources based on diluted magnetic III-V semiconductors.

He joined the University of California at Los Angeles (UCLA), Los Angeles, as a Postdoctoral Research Fellow in 2005. From 1995 to 1997, he was with Isfahan Optical Industry and was engaged in research and development of microelectronic circuits and DSP systems in Pardisan Inc. in 1998. He is currently a Visiting Assistant Professor at UCLA, researching on silicon photonics, particularly applications of nonlinear optical effects in active silicon optoelectronic devices. His research at UBC was on nitride heterojunction bipolar transistors. He is a coauthor of about 50 journal and conference publications.

Dr. Fathpour won the 2007 UCLA Chancellor's Award for Postdoctoral Research.

Bahram Jalali is a Professor of electrical engineering and the Director of the Optoelectronic Circuits and System Laboratory at University of California at Los Angeles (UCLA), Los Angeles.

From 1988 to 1992, he was a Member of Technical Staff at the Physics Research Division of AT&T Bell Laboratories, Murray Hill, NJ, where he conducted research on ultrafast electronics and optoelectronics. His current research interests are in silicon photonics and time-wavelength techniques for data processing and sensing. He has published over 200 scientific papers and holds 6 US patents. While on leave from UCLA from 1999–2001, he founded Cognet Microsystems, a Los Angeles based fiber optic component company. He served as Company's CEO, President and Chairman, from the company's inception through its acquisition by Intel Corporation in April 2001.

Dr. Jalali is a Fellow of the Optical Society of America (OSA) and the Chair of the Los Angeles Chapter of the IEEE Lasers and Electro Optics Society (LEOS). He is the recipient of the R.W. Wood Prize from the OSA. In 2005, he was chosen by the Scientific American Magazine as the 50 Leaders Shaping the Future of Technology. He is a member of the California Nano Systems Institute (CNSI). He has received the BridgeGate 20 Award for his contribution to the southern California economy. From 2001—2004, he served as a consultant to Intel Corporation. He serves on the Board of Trustees of the California Science Center.

Ernst Brinkmeyer received the Diploma and Doctoral degrees in physics from the University of Göttingen, Göttingen, Germany, in 1973 and 1976, respectively.

He is currently a Professor in the Electrical Engineering Department, Technische Universität Hamburg-Harburg, Hamburg, Germany, where he heads the Optical Communication Technology group. His current research interests include optical communications and optical instrumentation, in particular, Raman amplification, fiber Bragg gratings and planar UV-written structures, PMD compensation, and silicon photonics.